Mechanical characterization of meso-porous alumina by micro- and nano-indentation

Marwa Moula, Sylvain Meille, Vincent Le Corre, Jérome Chevalier

Mechanical characterization of meso-porous alumina by micro and nano-indentation

Marwa MOULA[1,2], Sylvain MEILLE [2,] Vincent LE CORRE [1], Jérôme CHEVALIER [2]

1 IFP Energies Nouvelles – Rond-point de l'échangeur de Solaize 69360 Solaize - France

2 Univ Lyon, INSA-LYON, MATEIS, UMR CNRS 5510, F69621 Villeurbanne, France

Abstract

Meso-porous γ-alumina ceramics used as catalyst supports are characterized by high porosity fraction (>70%) and specific surface area (>200 m^2/g) targeted to ensure high catalytic performances, but at the expense of the mechanical strength. The aim of this work is to link the mechanical properties of three different catalyst supports with their microstructure. Instrumented indentation tests were performed at two different length scales to assess mechanical properties at both macroscopic scale (support) and at constituents scale (grains and matrices). The distribution of porosity fraction in grains and matrices is estimated with image processing on Scanning Electron Microscopy (SEM) pictures. The mechanical behavior of catalyst supports are strongly influenced by their microstructure. In spite of a larger porosity fraction, macro-and meso-porous grains exhibit higher mechanical properties than the matrices. Matrix of the three alumina supports have almost similar volume fraction of porosity but different mechanical properties. Finally, Focused Ion Beam (FIB) cross-sections of residual indents indicate a damageable behavior under contact loading, with densification of larger pores.

Keywords: Catalyst support; Porous ceramics; Nano-indentation; Mechanical behavior; Densification

1 Introduction

Meso-porous alumina (γ-Al_2O_3) is a class of porous ceramics largely used in refinery industry as catalyst supports. γ-alumina is particularly used in hydrotreating processes of heavy oil fractions in fixed bed reactor [1]. Alumina supports can provide a large range of porosities and specific surfaces suitable for many catalytic applications. The influence of the microstructure of the support is experimentally observed for activity, selectivity, and deactivation of the hydrotreating process [2]

Over the past decades, many researchers have been focusing on the optimization of catalytic performances of alumina supports by maximizing their porosity and specific surface. However, an increase of porosity induces a decrease of the mechanical properties, which have a direct impact on the activity of the catalyst and the reactor. During transport and in-service life, catalyst supports are submitted to several mechanical stresses such as multi-axial compression, bending and shearing. Mechanical failure of the support results in the creation of fine particles causing the obstruction of filters, misdistribution of fluid flow, or even reactor shutdown [3]. Therefore, the mechanical strength of alumina supports should be one of the key parameters to achieve high performances in industrial reactors [4].

To the best of our knowledge, available articles in literature focus only on the brittle fracture of catalyst supports when subjected to tensile stresses. It has been shown that the primary reason for the mechanical failure is due to a brittle fracture of the catalyst supports arising from a sudden

growth of a critical flaw under tensile stresses, in agreement with the Griffith theory [5]. Recently, Staub et al. [6] studied the mechanical behavior of catalyst supports via three-point bending tests. Their work demonstrated that brittle fracture is initiated on macro-defects and heterogeneities present in the microstructure.

Otherwise, as catalyst supports are submitted to multi-axial compression during the production process, Staub et al. [7] studied the mechanical behavior of catalyst supports under multi-axial loads by spherical indentation. A quasi-plastic behavior with densification of materials was noted. The collapse of large pores was shown as being responsible for the densification phenomenon. When porous alumina are submitted to compressive loads, a brittle to quasi-plastic transition is detected while increasing the triaxiality of the stress state, i.e., the ratio of the iso-static-pressure to the equivalent shear stress. Under multi-axial compressive stresses, small cracks homogenously distributed extend stably. The coalescence of cracks induces the final fracture. The behavior of alumina with a porosity fraction above 50% is similar to that described for cellular ceramics [8], which exhibit a quasi-plastic damage with a fracture of solid walls between pores inducing pore collapse and densification mechanisms [9].

Unlike conventional mechanical tests, indentation test is well adapted to small specimens with a non-standard geometry. For this reason, this technique was used to characterize bone substitutes [10], shale [11], catalyst supports [7]. In particular, spherical indentation tests generate an elastic contact at low loads and allow studying the elastic-plastic transition as contact stresses increase with penetration depth [12,13].

Instrumented indentation can be carried out at different loads to characterize materials at different length scales. Indentation with high loads reveal an average response of the material while indentation with low loads produces shallow indents to characterize the local mechanical behavior of its components (grains, matrix, inclusions, etc) [11,14]. To identify mechanical properties of each entity in the heterogeneous materials, Constantinides et al. [15] proposed an approach to choose carefully the indentation length scale. In order to apply continuum indentation analysis to heterogeneous systems, the indentation depth has to be much smaller than the characteristic size of the microstructure. A rule established by Buckle [16] on coated system estimates that the indentation depth h should be at most 1/10 of the characteristic size D of the entity to be tested. Researchers [17,18] have also shown that the maximum indentation depth should be 5 times larger than the RMS of roughness of the sample to limit the influence of the surface roughness on the measured properties.

The objective of this study is to characterize the mechanical behavior of catalyst support at two scales, the macroscopic scale (support) and the microscopic scale (microstructure of the support) in order to understand the relationship between microstructure and mechanical behavior. To do so, microstructural characterization was first carried out using mercury intrusion porosimetry and imagery techniques. Then, spherical and pyramidal micro-indentation tests were performed to study the average macroscopic behavior of the material. Three points bending tests were also performed to estimate the strength bending of catalyst supports. At the microscopic scale, pyramidal nano-indentation tests were used to qualitatively assess the mechanical properties of the constituents of the material. In this work, three different meso-porous γ-alumina supports of similar porosity fraction but different microstructures were studied in order to analyze the influence of the morphology on the mechanical properties of industrial catalyst supports.

2 Materials and methods

2.1 Background on catalyst support microstructures

Meso-porous alumina catalyst supports are usually synthesized through thermal treatments of boehmite. In a typical synthesis process, boehmite powder is first dispersed in solvent. The suspension is mixed and the support pellets are extruded. The extrudates are then calcined under air to obtain porous transition alumina. The microstructure of alumina support is composed of grains dispersed in matrix. The matrix is obtained by the dispersion of the boehmite powder under acid solution and mechanical action performed by kneading. This action breaks the agglomerates to form nanoscale aggregates. As reported in [19,20], the matrix is constituted by aggregates obtained from the stacking of elementary nanocrystals of alumina. A first scale of porosity called “intra-aggregate porosity” is found between alumina nanocrystals as shown in *Figure 1*. Aggregates are held together to form agglomerates of a few tens of microns also referred as grains. Hence, a second scale of porosity exists in between aggregates called “inter-aggregate porosity”.

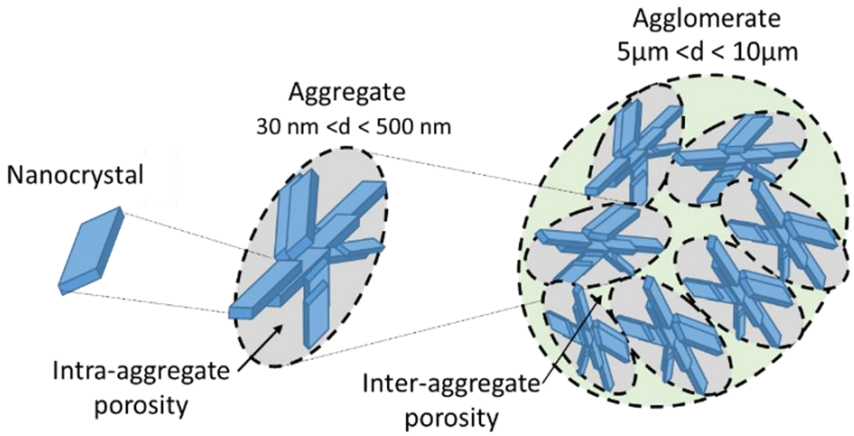

Figure 1: Schematic representation of the microstructure components of alumina support. Agglomerates with inter-aggregate porosity are grains with macro-mesoporosity

2.2 Catalyst supports samples

Three γ-alumina supports, provided by IFPEN (Solaize, France), were studied in this work. Supports were obtained by precipitation of aluminum salts in an aqueous solution. The boehmite precipitate was filtered, washed and dried by atomization. Shaping involves the passage from a boehmite powder to support pellets. First, a boehmite paste was obtained by kneading the powder with an acid solution, followed by a basic solution for the neutralization. The paste was then extruded through a die with a unique cylindrical hole. Subsequently, extrudates were dried and calcined. Their diameter ranged from 1.2 to 1.4 mm and their final length from 2 to 6 mm. Three material formulations were studied, with different capacities of dispersion of the boehmite aggregates. Moderate, high, and very high dispersion of the boehmite provided different microstructures of the final alumina, respectively noted MD, HD and THD. The final γ-alumina supports had a purity > 99% by weight. Alumina supports were selected to have very similar total porosity fraction in order to investigate the influence of microstructure features on mechanical properties.

2.2.1 Observation of samples microstructure

Observations of the microstructure of samples were carried out by Scanning Electron Microscopy (SEM) with a Supra 40 SEM (Zeiss, Germany). Surfaces were first impregnated with epoxy resin and then carefully mechanically polished with diamond papers down to 1 µm. For high-resolution observations, the surface of samples was prepared by electro-polishing using an Ilion II polisher from Gatan with a voltage of 6 kV for 6 hours.

2.2.2 Textural analysis

2.2.2.1 Total porosity

Textural properties were estimated from nitrogen adsorption and mercury porosimetry. The data obtained from these methods are usually analyzed by assuming that the porous material contains inter-connected cylindrical pores. Nitrogen isotherm is used to estimate the surface area S_{BET} [21] produced by pores which diameter is ranged between 2 and 50 nm. The pore size distribution is estimated from the BJH method [22].

Mercury intrusion porosimetry is a complementary technique to nitrogen absorption, it can achieve macroporosity (< 50 nm) and mesoporosity (between 3.6 and 50 nm). This technique provides the total pore volume $V_p$and the pore size distribution. The median pore interconnection size is defined as the size corresponding to 50% of the mercury volume intruded. In addition, the apparent grain density ρ_b was measured at very low intrusion pressure of mercury (0.2 MPa). At this pressure, mercury surrounds the sample without entering in the porosity and the volume of the sample can be estimated.

Helium pycnometry provided the structural density ρ_s. The porosity *P* of the alumina supports was calculated using the structural density ρ_s and the grain density ρ_b as the following expression:

$$P = 1 - \frac{\rho_b}{\rho_s} \qquad \textbf{Equation 1}$$

2.2.2.2 Grain size distribution

The mean grains diameter of each material was estimated by image processing using Fiji software [23] using several SEM images. These latter were obtained from the observation of polished sections after (methyl metacrylate) resin impregnation using Back-Scattered Electron (BSE) imaging mode. The image processing consisted first in applying a thresholding on images. The threshold gray level is adjusted in order to maximize the entropy of the image which means the information measure between the objet and background composing the image. An automatic analysis of particles was then applied to segmented images in order to determine the surface fraction of grains and the diameter of each of them.

2.2.2.3 Volume fraction of local porosities

Local porosities in the matrix and in the grains were estimated via image processing on SEM images of each material. SEM images used to determine the grain size distribution (section 2.2.2.2) were also

used to estimate local porous volume fraction by a quantitative image analysis, based on contrast ratios. In the BSE mode, it is considered that brighter areas have a higher mean atomic number [24]. Indeed, numerous experimental studies show that the backscattered coefficient η, which is conventionally defined as the ratio of the number of electrons that backscatter out of the sample surface to the total number of the incident electrons, is highly sensitive to the mean atomic number Z. Reimer et al. [24] proposed the following analytic expression to link η and *Z*:

$$\eta = -0.0254 + 0.016Z - 1.86\,10^{-4}Z^2 + 8.3\,10^{-7}Z^3 \qquad \textbf{Equation 2}$$

Summing rules were proposed in the literature for calculating mean atomic number *Z* of a chemical compound specimen. Büchner's rule, presented in Equation 3 , was used in this work, as it is better adaptable for backscattered electron signal [25,26].

$$\bar{Z}^2 = \sum_{i=1}^{N} a_i {Z_i}^2 \qquad \textbf{Equation 3}$$

which a_i and Z_i are respectively the atomic concentration and atomic number of the element *I*. The calculated mean atomic number of resin Z_r and alumina Z_a are respectively 4.6 and 10.3, which indicates higher backscattered coefficient η for alumina. Therefore, the darker grey value is referred to pure resin which represents the porosity and the brighter grey value is referred to pure alumina. The variation of the backscattered coefficient η with the mean atomic number between pure resin and pure alumina can be considered as linear.

If the contrast of the image is such that the local grey value is equal to zero for the pure resin (for instance in a macropore or in a crack), a linear relation between the local grey value and the local atomic number at each pixel *x* in the image can then be written in the form:

$$Z(x) = \frac{Z_m - Z_r}{g_m}\, g(x) + Z_r \qquad \textbf{Equation 4}$$

where Z_m and g_m are respectively the mean atomic number and the mean grey value in the image.

Moreover, the mean atomic number of each pixel can be written as a function of the atomic concentration a_r of the resin as follows:

$$Z^2(x) = {Z_r}^2 a_r(x) + {Z_a}^2 \left(1 - a_r(x)\right) \qquad \textbf{Equation 5}$$

The atomic concentration can be expressed as a function of the porosity rate P as follows:

$$P(x) = \frac{\alpha a_r(x)}{1 + (\alpha - 1)a_r(x)} \qquad \textbf{Equation 6}$$

with $= \frac{\rho_a \mathcal{M}_r}{\rho_r \mathcal{M}_a}$, $\mathcal{M}_a$ the alumina molar mass, ρ_a the alumina density, $\mathcal{M}_r$ the resin mass molar and ρ_r the resin density.

Combining Equations 4 and 5, a new expression of the porosity fraction *P* of each pixel can be obtained:

$$P(x) = \frac{\alpha \frac{(Z^2(x) - {Z_a}^2)}{({Z_r}^2 - {Z_a}^2)}}{1 + (\alpha - 1)\frac{(Z^2(x) - {Z_a}^2)}{({Z_r}^2 - {Z_a}^2)}}$$ **Equation 7**

The final relation between the porosity and the grey values, obtained by combining Equation 4 and Equation 7, is not linear. The mean atomic number of the image Z_m is iteratively calibrated such that the mean porosity rate corresponds to the porosimetry estimation (Equation 1). Then, thanks to masks of segmented images (2.2.2.2), the mean porosity of grains and matrices are computed.

2.3 Three points bending

The bending strength was measured with a Bose Electro-Force® test instrument (Prairie Valley, USA) equipped with a 20 N load cell. 32 extrudates of each material were tested. The span between the two lower supporting rolls was set to 15 mm. The samples chosen were longer than 15 mm (*Figure 2*).

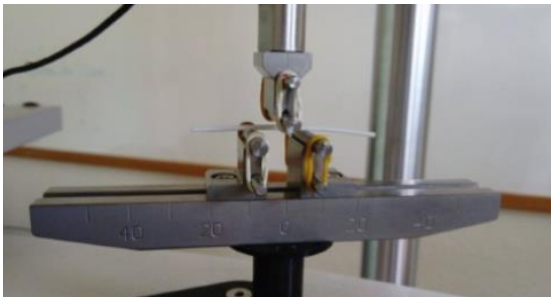

Figure 2: Three-point bending test performed on a cylindrical support

The maximum tensile stress in the middle of the sample can be calculated from the following equation [27]:

$$\sigma_r = \frac{8F_r L}{\pi d^3}$$ **Equation 8**

where F_r is the applied load, *L* is the span between the lower load points and *d* is the diameter of the sample. In addition, Young's modulus can be calculated from [27]:

$$E_{3PB} = \frac{4L^3}{3\pi d^4}\frac{dF}{du}$$ **Equation 9**

with *u* the deflection of the sample.

2.4 Indentation tests

2.4.1 Background on instrumented indentation methods

The load–displacement curves were analyzed considering elastic-plastic loading and purely elastic unloading [28]. The initial unloading slope is defined as the contact stiffness *S* expressed as a function of the reduced Young's modulus E_r [29] as following:

$$S = \frac{2\beta}{\sqrt{\pi}} E_r \sqrt{A_c(h_c)} \qquad \textbf{Equation 10}$$

Where h_c is the contact depth, β is a constant depending of indenter geometry (1 for sphere and 1.034 for Berkovich) and A_c is the projected contact area. The modulus E_r was determined from the relation:

$$\frac{1}{E_r} = \frac{1-\nu^2}{E} + \frac{1-\nu'^2}{E'} \qquad \textbf{Equation 11}$$

where E, ν and E', ν' refer to the Young's modulus and Poisson's ratio of the sample and of the indenter respectively.

Indentation hardness was calculated using the following equation [32]:

$$H = \frac{P}{A_c} \qquad \textbf{Equation 12}$$

where A_c is the projected contact area and *P* is the applied load.

2.4.1.1 Spherical indentation

In the case of spherical indentation, by applying the Sneddon equation [28,30], the reduced modulus E_r can be defined as following [33]:

$$E_r = \frac{S}{2\,a} \qquad \textbf{Equation 13}$$

where *a* is the radius of contact and $A_c = \pi a^2$.

Spherical indentation testing can be used to study the elastic-plastic transition in a material since the contact stresses increase with the penetration depth. The indentation stress-strain behavior can be analyzed by plotting the mean pressure $P_m = {}^{P}/_{\pi a^2}$ as a function of the indentation strain ${}^{a}/_{R}$. This relation is represented by the following expression [31]:

$$\frac{P}{\pi a^2} = \frac{4}{3\pi} E_r \frac{a}{R} \qquad \textbf{Equation 14}$$

where *R* is the sphere radius.

2.4.1.2 Berkovich indentation

For a perfect Berkovich indenter, the projected contact area, A_c, is a function of the contact depth h_c, and it is expressed as follows:

$$A_c = 24.5\, {h_c}^2 \qquad \textbf{Equation 15}$$

In contrast to spherical indentation, Berkovich indentation testing cannot be used to study the elastic-plastic transition but it allows to explore wide range of pressure during indentation.

2.4.2 Experimental information

All indentation experiments were performed with a G200 nanoindenter (Agilent Technologies, Chandler, USA) equipped with a Continuous Stiffness Measurement (CSM) module. Both Berkovich and spherical indenters were used.

2.4.2.1 Spherical micro-indentation

Spherical indentation test was carried out at macro scale to characterize the average mechanical behavior of the three alumina supports. A sapphire spherical indenter tip was used with a nominal radius of 354 µm. The samples were first embedded in a resin to be maintained in a stable and upright position. Resin used for embedding is a very viscous resin (KM-U methyl methacrylate based resin, Presi) to avoid impregnation of pores. Embedded samples were then mechanically polished using diamond suspension down to 1 µm. Surface roughness R_a measured for the three materials was estimated to 800, 700 and 500 nm for MD, HD et THD alumina supports respectively.

Indentation tests were performed to a maximum load of 1200 mN leading to a maximum penetration of 5 µm. The strain rate was chosen to be 0.05 s^{-1}. The load was maintained at its maximal value during 10 s before unloading. Four indentations were realized on each sample. The distance between indents was equal to 400 µm. The interaction between indents was neglected since the mean contact radius was around 90 µm.

2.4.2.2 Berkovich micro-indentation

Pyramidal indentation tests were performed to investigate the average mechanical properties of catalyst supports using a sharp diamond Berkovich indenter. The maximum load was fixed to 1200 mN, leading to a maximal penetration of 15 µm. The strain rate was equal to 0.05 s^{-1}. More than five indentations were performed for each material.

2.4.2.3 Berkovich nano-indentation

Nano-indentation tests with a Berkovich tip were performed with low applied loads to investigate the mechanical properties of the grains and matrices of the three alumina supports. The choice of the Berkovich indenter is related to its insensitivity to roughness. The samples were prepared by an electro polishing Ilion (Gatan, Europe) with a tension of 6 kV during 6 hours as for the SEM observations. The polished area is representing approximately one third of the extrudate cross-section. This technique allows to have a fine preparation of surface, revealing the microstructure of the alumina support. Before each series of nano-indentation tests, the polished surface was observed with SEM in order to determine the locations of the grains (and therefore of the matrix) to be tested. The characteristic size of grains tested with nano-indentation is larger than 5 µm as smaller grains requires an ultra-low load nano-indentation (< 1 mN), not adapted to the equipment. Therefore, the matrix tested in nano-indentation is composed of the homogenous part of the microstructure and small grains, lower than 5 µm in equivalent diameter.

Based on the rule of Buckle [16], the maximum penetration depth was chosen referring to the characteristic size of the grains to test. It was fixed to 400 nm for all the nano-indentation tests.

The maximum indentation depth was at least 4 times more than the surface roughness R_a of samples (< 100 nm) after electro-polishing. Nano-indentation tests were performed under a constant deformation rate of 0.05 s^{-1}. Positioning the indents was done with the optical microscope unit of the nanoindenter. After testing, each indentation locus was examined individually by SEM to check that indents are positioned correctly in targeted grains or in the matrix.

2.4.2.4 Profiles of residual indents

Profiles of residual indents after Berkovich nano-indentation were measured by an atomic force microscope (AFM) Bruker Dimension 3100 (California, United States) and a FIB/SEM (NVision 40 of Zeiss) cross-section of an indentation was realized in order to identify the deformation mechanism of the material under compression and to detect potential damage and densification.

3 Results

3.1 Microstructure

3.1.1 SEM observation

Figure 3 reveals the microstructure of the three materials, in the form of randomly distributed grains in a continuous matrix. As surfaces are resin-impregnated, the porosity appears in black in the SEM images and the difference of contrast is linked to the difference in density. The microstructure of the sample MD is composed of grains with different sizes dispersed in matrix. Two types of grains are detected in the microstructure (*Figure 3a* and *b*). Grains which appear darker contain two scales of porosity: intra- and inter-aggregate porosity as presented in *Figure 1.* These grains referred hereafter as “macro- and meso-porous grains”. Brighter and denser grains hereafter referred as “meso-porous grains” which contain only the intra-aggregate of porosity. The HD sample is characterized by small grains distributed in the matrix (*Figure 3c and d*). In some areas, these grains are agglomerated to constitute larger “macro- and meso-porous grains”. These grains appear as more homogenous contrast than in “macro- and meso-porous grains” of the MD sample. The THD sample appears less heterogeneous (Figure 3*e and f*) as compared with samples MD and HD, with grains appearing brighter i.e., denser, than the matrix. A decohesion is observed between these grains and the matrix.

As presented in *Figure 4*, the alumina supports have different grains size distributions. The mean diameter (corresponding to the highest probability in *Figure 4*) is estimated to 1.2 µm for “meso-porous” grains of the MD sample and circular grains of the THD sample. The mean diameter of large “macro-and meso-porous” grains of the sample HD and the sample MD is around 2.5 µm.

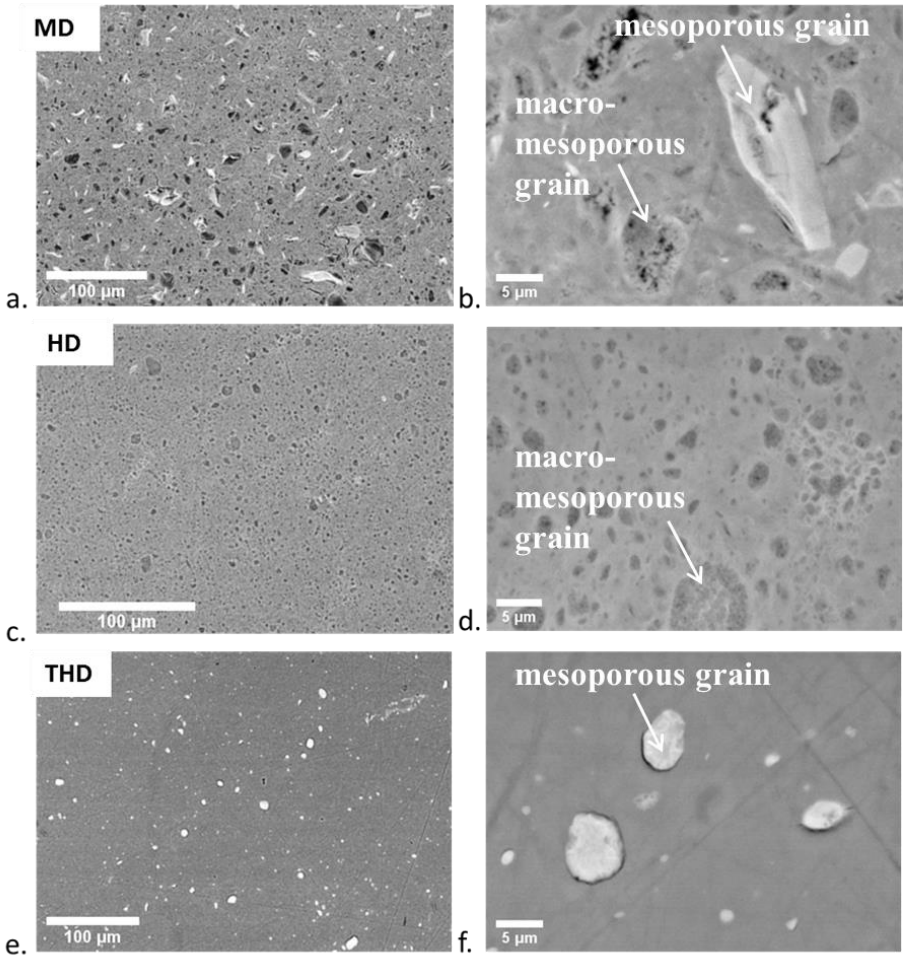

Figure 3 : SEM observation (Backscattered Electron Imaging mode), at two magnifications, of polished section after resin impregnation of three materials, (a, b) MD, (c, d) HD and (e, f) THD.

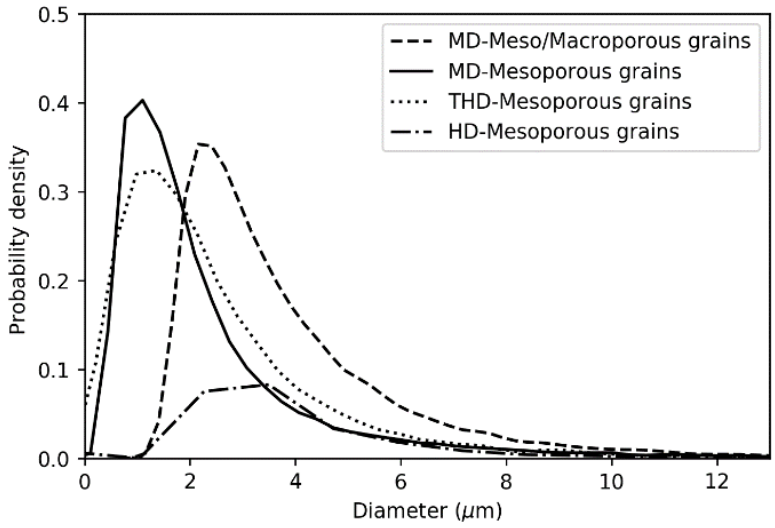

Figure 4: Distributions of grain size in the three alumina supports using the probability density function

3.1.2 Total porosity

Table 1 summarises different microstructural properties of the three catalyst supports. The specific surface area S_{BET} varies slightly between 302 and 283 $m^2 g^{-1}$. The total pore volume fraction *P*, the pore diameter, *d*, and the structural density ρ_s are similar for all three supports. The pore size distributions are reported in *Figure 5*. The three alumina supports have a bimodal pore size distribution. Their interconnection pore size distribution varies significantly between 5 and 15 nm.

Table 1: Alumina supports textural properties

Alumina support	$S_{BET}(m^2 g^{-1})$	d (nm)	$\rho_s(\mathrm{g}.cm^{-1})$	P (%)
MD	302 ±15	9.5	3.20	69.9 ±0.2
HD	283 ±14	8.4	3.22	70.8 ±0.1
THD	286 ±14	8.9	3.24	70.4 ±0.3

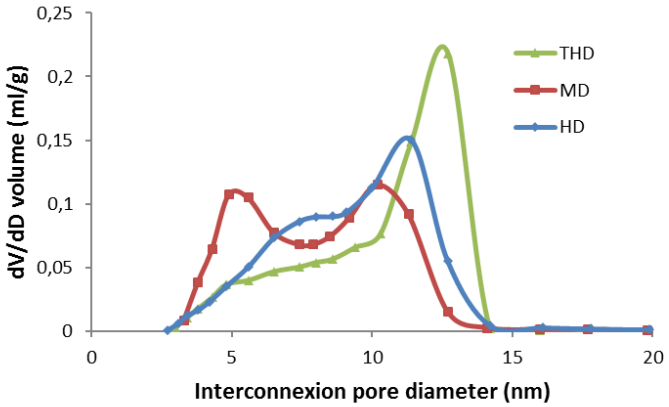

Figure 5: Pore size distribution estimated by the BJH method

3.1.3 Estimation of porous volume fraction of grains and matrices

30 images were realized by SEM using the same observation conditions (working distance, tension, contrast, brightness, etc.) on the three alumina supports. Applying the method based on image-processing detailed in the section 2.2.2.3, mean values and standard deviations of the volume fractions of grains and matrices were estimated and are given in *Table 2*. The surface area fraction of grains and matrices is supposed equivalent to their volume fraction (hypothesis of an isotropic microstructure supported by *Figure 3*). For the three alumina supports, the volume fraction of grains is less than 10%. Values for the alumina support HD are more scattered than for MD and THD samples. Very few micro-cracks are detected on SEM images.

Local porosities in grains and matrices are estimated in *Table 3*. The three alumina supports have similar porosity fraction however its components exhibit different porous volume fraction. The macro-and meso-porous grains are more porous than the meso-porous grains and that the matrix.

Table 2: Volume fraction of matrices and grains for the three alumina supports

Volume fraction (%)	Matrix	Macro-meso-porous grains	Meso-porous grains	Cracks
MD	89.7 ±1. 2	7.05 ±1.1	2.95 ±0.1	0.3
HD	96.2 ±4.2	3.56 ±4.0	/	0.2
THD	96.9 ±0.8	/	2.41 ±0.9	1.4

Table 3: Porous volume fraction of grains and matrices for the three alumina supports

Porous Volume fraction %	Matrix	Macro-meso-porous grains	Meso-porous grains
MD	73.9 ±0.1	79.0 ±0.7	62.2 ±0.1
HD	71.7 ±0.3	79.3 ±0.8	/
THD	77.1 ±0.4	/	/

3.2 Bending strength

During the test, catalyst supports were snapped into two parts at the center load point. The maximum tensile stress at fracture and Young's modulus, presented in *Table 4*, were calculated using Equation 8 and Equation 9. The maximum tensile stress and Young's modulus are lower for THD support than for MD and HD supports. The properties of HD support are more scattered than those of MD and THD supports.

Table 4: Maximum tensile stress at fracture and Young's modulus measured with three bending tests on the three catalyst supports

Alumina support	σ_r(MPa)	E_{3PB}(GPa)
MD	12.8 ±1.6	5.7 ±0.6
HD	11.1 ±2.4	4.8 ±1.4
THD	7.5 ±1.7	3.1 ±0.4

3.3 Spherical micro-indentation

Figure 6 presents typical load-displacement curves during spherical micro-indentation for the three materials. Furthermore, Figure 6 illustrates the differences noted between the three alumina. The

maximum penetration depth h_{max} in each material was respectively 6.5 µm, 7 µm and 10 µm for MD, HD and THD supports. The residual penetration depth was around 3.6 µm for MD and HD and 5 µm for THD. Two small plateaus were observed in Figure 6.a at 600 mN (corresponding to the switch from low to high load mode of the nanoindenter) and at the maximum load of 1200 mN (dwell of 10 s) indicating of the existence of a time dependent viscous deformation in the materials.

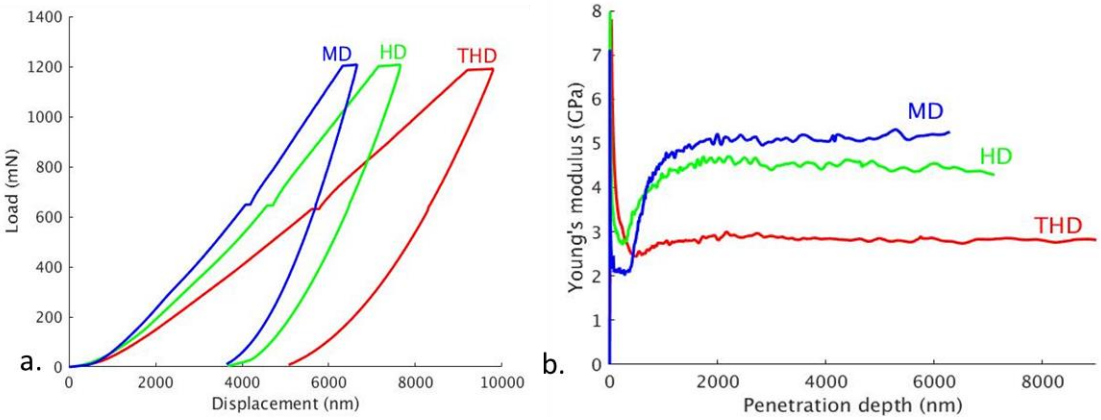

Figure 6: a) Typical Load-displacement and b) Young's modulus-penetration depth curves of the three alumina supports. The load was maintained at 600 mN during 10 s to allow the change from the "low load" to the "high load" method

The evolution of apparent Young's modulus as a function of the penetration depth for the three-alumina supports is plotted in *Figure 6.b*. For the indentation depth of less than 1.5 µm, curves indicate a progressive setting of the contact between the tip and the material related to the roughness of the surface. Young's modulus stabilized depths deeper than 1.5 µm, until the end of the test. CSM mean values were thus calculated for penetration depths between 3 and 6 µm. Mean values and standard deviation of Young's modulus are given in *Table 5*, as determined by CSM, O&P and 3 points bending tests respectively. CSM modulus are close to those evaluated by Oliver & Pharr (O&P) method and lower than 3 points bending modulus. A slight dispersion of results for each material was noted, probably due to some spatial heterogeneity of the alumina supports.

Table 5: Mean values of Young's moduli obtained by spherical micro-indentation tests (either CSM or Oliver & Pharr and three-Point-Bending). They are noted respectively $\mathbf{E_{CSM}^{Sph}}$, $\mathbf{E_{O\&P}^{Sph}}$, $\mathbf{E_{3PB}}$

Alumina support	E_{CSM}^{Sph} (GPa)	$E_{O\&P}^{Sph}$ (GPa)	E_{3PB}(GPa)
MD	5.0 $\pm$0.4	5.0 $\pm$0.4	5.7 $\pm$0.6
HD	4.7 $\pm$1.3	4.2 $\pm$1.2	4.8 $\pm$1.4
THD	2.6 $\pm$0.3	2.7 $\pm$0.2	3.1 $\pm$0.4

Figure 7 shows the indentation stress-strain curves for the three alumina supports obtained during spherical indentation. As described in section 2.4.1, P_m is the indentation stress and a/R is the

indentation strain. The stress-strain curves present three domains. For *a/R* less than 0.02, curve is non-linear due to the stabilization of the initial contact between the indenter and the surface. This stabilization is detected by the progressive setting the curve of the apparent Young's modulus for depths less than 1.5 µm corresponding to a/R less than 0.02 (*Figure 6.b*). The next domain is linear and corresponds to the elastic contact described by Hertz contact theory. The last domain is non-linear and defines the transition between the elastic and elasto-plastic contact. Thus, it is possible to determine the mean contact pressure P_m at transition corresponding to the beginning of the damage. The indentation stress at the end of the elastic regime is estimated to 78 MPa, 40 MPa, and 32 MPa for MD, HD, and THD respectively.

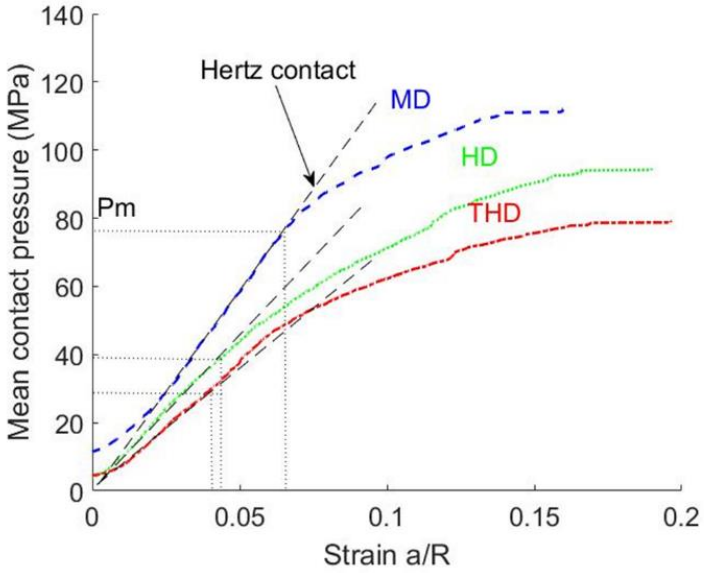

Figure 7: Typical indentation stress-strain obtained during spherical micro-indentation of the three alumina supports.

3.4 Berkovich micro-indentation

Load-displacement curves recorded during Berkovich micro-indentation of the three materials with a maximum load of 1200 mN are shown in Figure 8.a. The shape of the curves is similar to the one noted in spherical micro-indentation tests (Figure 6), however, the residual penetration in Berkovich tests is two times higher than after spherical micro-indentation for the same maximum applied load."

Figure 8.b presents Young's modulus versus penetration depth during spherical and Berkovich micro-indentation with a maximal load of 1200 mN. Both indentation types exhibit a progressive setting of the contact between the tip and the sample at the beginning of test because of the surface roughness. Then, Young's modulus becomes constant for depths deeper than 2 µm. Mean value of Young's modulus is calculated for the three alumina supports for depths between 2 µm and 16 µm. It is equal to 7.8 GPa for MD, 6.8 GPa for HD and 3.3 for THD (*Table 6*). Mean values of hardness and Young's modulus of Berkovich micro-indentation are higher than mean values obtained from micro-spherical indentation.

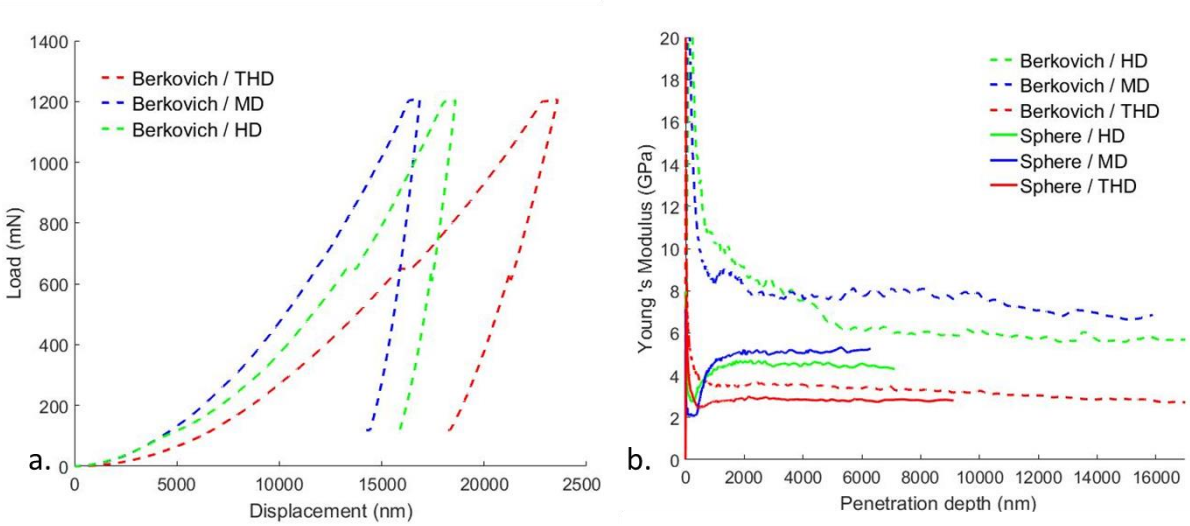

Figure 8: a) Typical load-displacement measured by Berkovich indenter. b) Young's modulus-penetration depth curves measured of the three-alumina supports by spherical and Berkovich indenter.

Table 6: Mean value and standard deviation of dynamic Young's moduli and hardness measured from series of spherical and sharp micro-indentation performed on the three-alumina support

Alumina support	E_{sph}(GPa)	E_{Berko}(GPa)	H_{Berko}(MPa)	P_m(MPa)
MD	5.0 $\pm$0.36	7.8 $\pm$0.30	280 $\pm$30	78 $\pm$5
HD	4.2 $\pm$1.2	6.8 $\pm$0.90	230 $\pm$30	40 $\pm$10
THD	2.7 $\pm$0.16	3.3 $\pm$0.48	150 $\pm$10	32 $\pm$6

3.5 Berkovich nano-indentation

As presented in section 3.1 , the alumina support MD is characterized by two types of grains: "macro-meso-porous grains" and "meso-porous grains". Series of nano-indentation tests were performed on the two types of grains and on the matrix on 4 different samples with a 400 nm maximum depth. The typical side length of the residual imprints was 2 µm. Each nano-indentation locus was examined by SEM. *Figure 9* shows a BSE image of the residual imprint into grains. For the support HD, matrix and agglomerated grains were tested. Eventually, only the matrix of the support THD was tested because of the decohesion between matrix and grains.

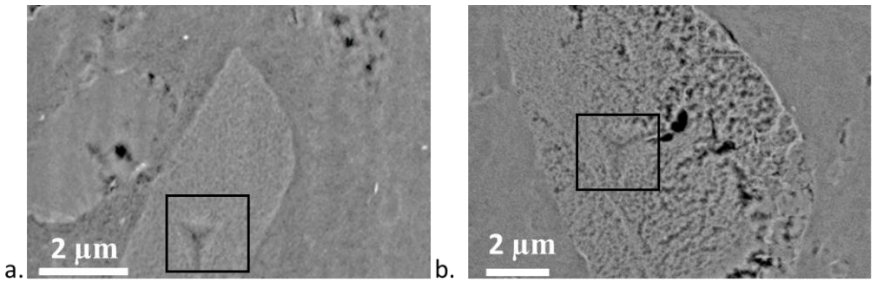

Figure 9: SEM observation with Backscatter electron (BSE) image of post-indented MD sample a) meso-porous grain, b) macro- and meso-porous grains

Figure 10 shows load-displacement curves obtained from 400 nm deep indents into the different constituent of each alumina support. The figure illustrates a different response of grains and matrix but also the experimental scatter within grains and matrix. For the material MD, the maximal load reached by the nano-indentation in "meso-porous grains" are two times higher than in "macro-meso-porous grains" and about three times higher than the matrix. Similarly, for the material HD, maximum load obtained by nano-indentation into agglomerated grains is higher than into matrix. The matrix of the material THD exhibits the lowest maximum load of all tests.

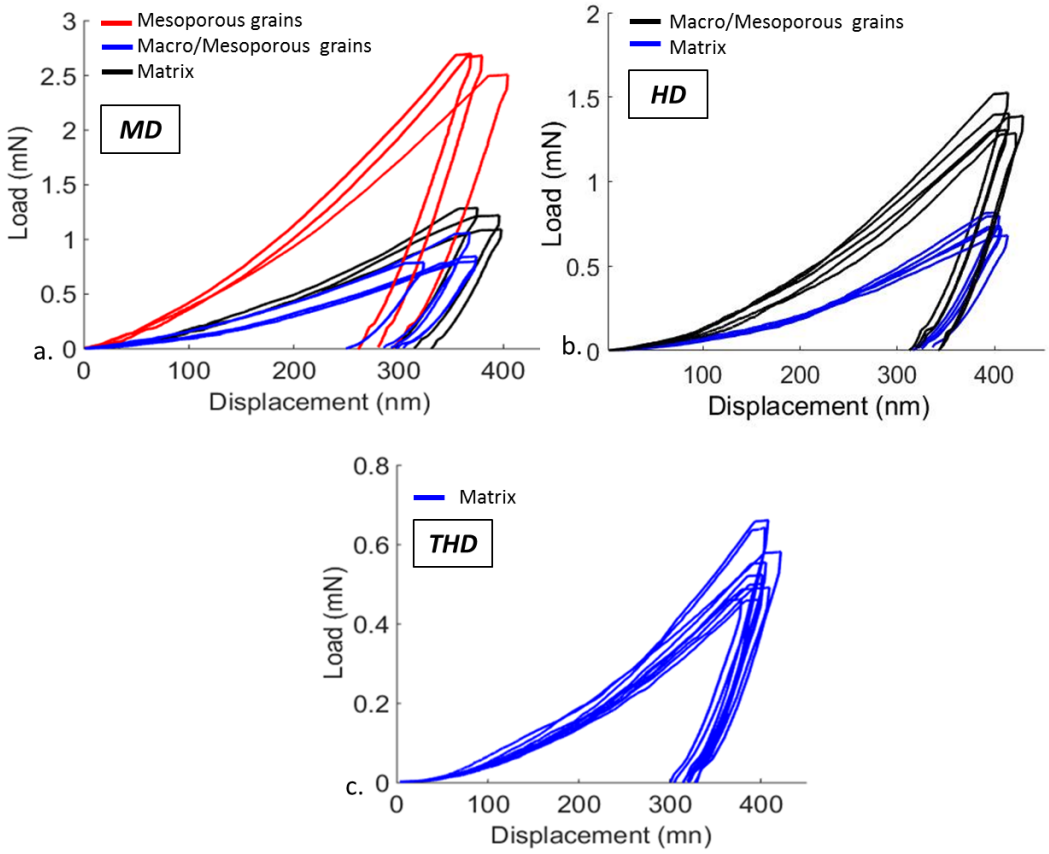

Figure 10: Load-displacement curves recorded during nano-indentation of constituents of each material: a) matrix (blue), macro-and meso-porous grains (black) and meso-porous grains (red) of the material MD, b) matrix (blue), grains (black) of the material HD, c) matrix of the material THD

Figure 11 presents the CSM Young's modulus versus penetration depth for constituents of the three alumina supports. For depth penetrations lower than 100 nm, curves show progressive setting of the contact, which indicates low surface roughness after ion polishing. Young's modulus starts to stabilize above 100 nm and remains stable until the end of the test. It can be noted that the Young's modulus obtained for meso-porous grains for the material MD is not completely stabilized at the end of the test. Mean values of the Young's modulus are calculated between 200 nm and 350 nm for all tests.

Table 7 shows the subsequently extracted mechanical properties for all entities. The elastic modulus and hardness were found to be higher in grains as compared with matrix. For the alumina support MD, the elastic modulus of meso-porous grains is estimated to 18.9 GPa, two times higher than the elastic modulus of matrix.

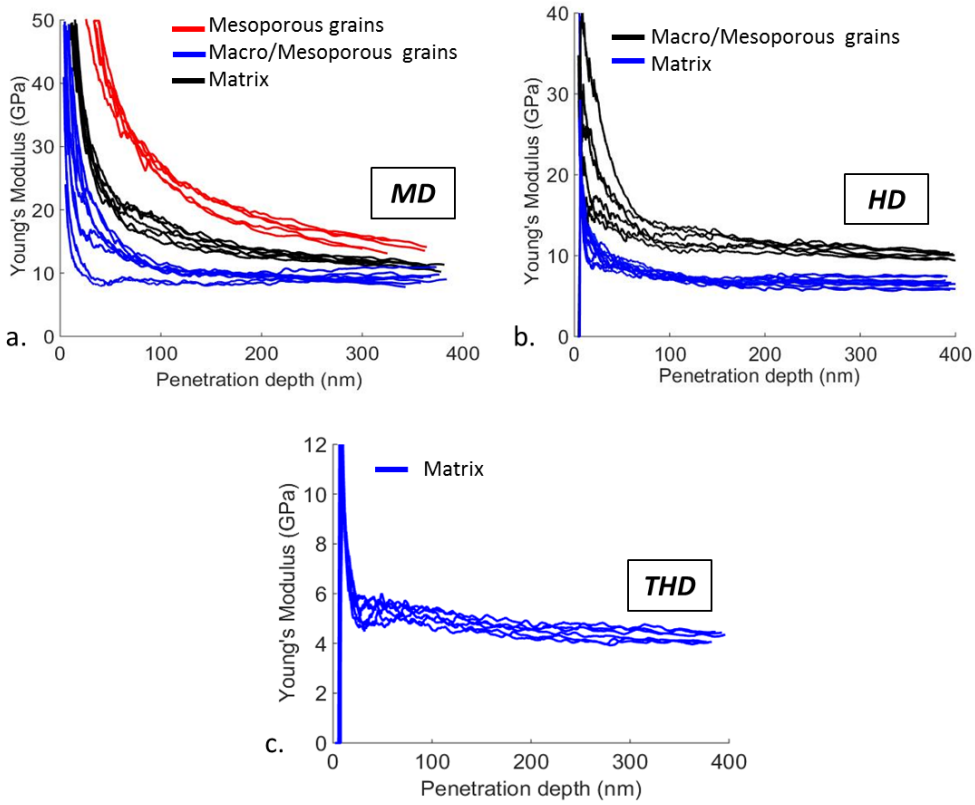

Figure 11: Indentation Young's modulus versus penetration depth recorded during nano-indentation of constituents of each material: a) matrix (blue), macro-and meso-porous grains (black) and meso-porous grains (red) of the material MD, b) matrix (blue), grains (black) of the material HD, c) matrix of the material THD

Table 7: Measured Young's modulus and hardness of grains and matrices (average ± standard deviation)

	E_{csm}(GPa)	H(MPa)
Meso-porous grains/MD	18.9 ±1.51	1300 ±220
Macro-meso-porous grains/MD	12.2 ±1.22	620 ±190
Grains/HD	11.2 ±0.78	510 ±60
Matrix/MD	9.5 ±1.32	410 ±80
Matrix/HD	7.1 ±1.06	330 ±70
Matrix/THD	4.8 ±0.86	220 ±50

3.6 Profiles of residual indents

Figure 12 shows the profile of indent mark after nanoindentation of matrix without any pile up. The observation of the surface and cross-section of nano-indentation demonstrated the absence of surface cracks at the corners of the indent. SEM observation of the cross section of residual indentation imprint in the matrix clearly highlights the existence of a densification zone below the residual imprint. Around the densified zone, mesopores appearing as dark inclusions with a spheroid shape are homogenously distributed in the matrix. In the densified zone, no more mesopores are visible. The depth of the densified volume is approximately equal to 500 nm (*Figure 13.c*)**.**

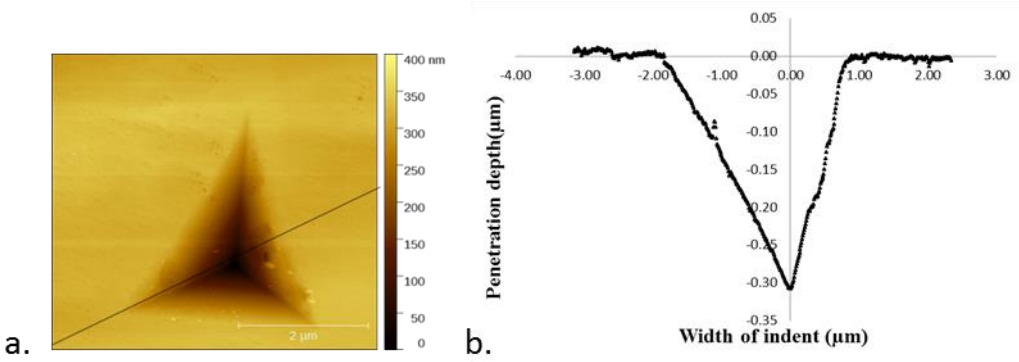

Figure 12:a) Example of AFM observation of 400 nm depth indentation on matrix of alumina support MD, b) Cross section profile at the position indicated by the line in (a)

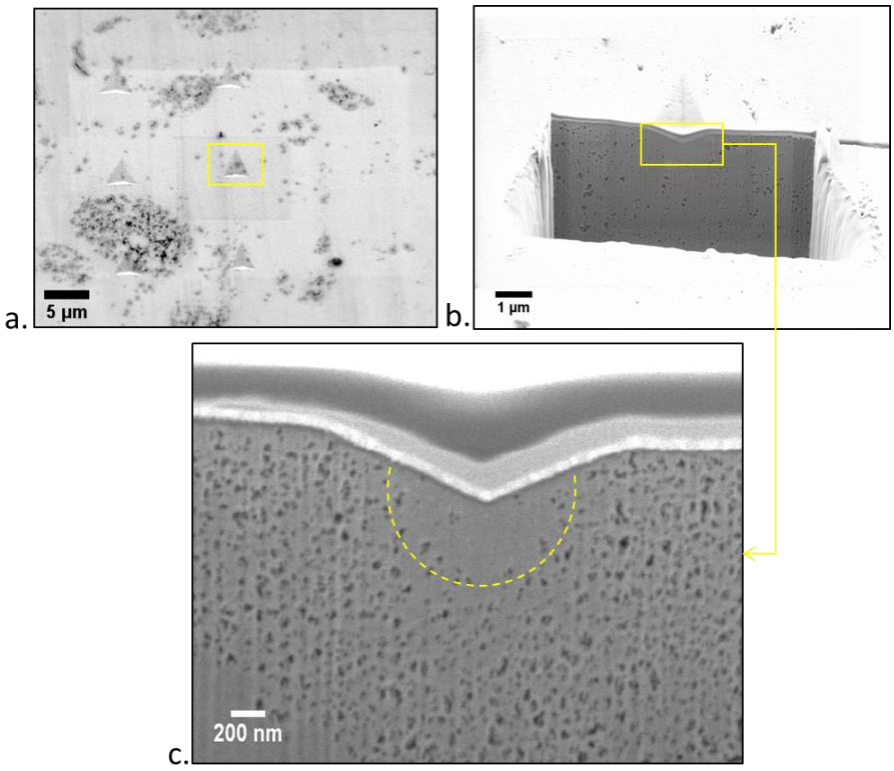

Figure 13: Surface of nano-indentations marks in matrix observed by SEM; b), c) FIB cross-section of nano-indentation marks in matrix (framed by a square) putting in evidence the densification

4 Discussion

4.1 Global mechanical behavior of alumina supports

4.1.1 Quasi-plastic behavior of alumina supports

As noted in the introduction, only a few studies in the literature have dealt with the micro-indentation of highly porous inorganic solids [7,12,13]. A quasi-plastic behavior has been observed under indentation on highly porous ceramics such as sintered hydroxyapatite [34], microporous plaster [12], foamed plaster [35] and porous alumina [7]. It is characterized by the development of a densified zone under the residual imprint without macro-crack propagation. Similar behavior is detected on the materials of our interest using indentation tests. The quasi plasticity is reflected in the stress-strain curve obtained during spherical micro-indentation (*Figure 7*). The curve shows a transition from linear to non-linear stress strain relationship which indicates the initiation of damaging beneath the indent.

The profile of the residual imprint (*Figure 12* and *Figure 13*) indicates the existence of residual plastic strain and disappearance of pores beneath the indent. Analysis of the damaged zone beneath the indent on macro-porous ceramics used as γ-alumina [7], plaster [12], brittle foam [35] and fuel cell electrode [36], clearly indicate the densification of the microstructure induced by the collapse of largest pores. It is very likely that the same phenomena is present in the studied material caused by microcracking mechanisms or micro-sliding of crystals and inducing subsequent pore collapse. For

this work, the average size of pores is much more smaller than those studied in the literature (*Figure 13.c*).

4.1.2 Micro-indentation using spherical and Berkovich indenters

Micro-indentation of alumina supports using Berkovich and spherical tips with the same maximum load (1200 mN) gives different results. Young's modulus measured from Berkovich micro-indentation is higher than Young's modulus measured from spherical micro-indentation. It has been seen that the residual penetration after Berkovich micro-indentation is two times higher than residual penetration obtained after spherical micro-indentation [37], this being related to the indenter tip shape. In sharp micro-indentation, a stress singularity exists from the beginning of the test, leading to plastic deformation, which results in partial closure of pores and densification. However, beneath the spherical indenter, stress concentration is smoother with an initial elastic stage followed by an elastic–plastic transition (Figure 7), the pore structure will be less damaged during the initial contact loads. It seems that the damage zone has an influence on the Young's modulus, the spherical elastic modulus being lower than modulus measured by sharp indentation [38,39]. It has been demonstrated via numerical simulation that spherical tests are much less sensitive to damage than the Berkovich test [37]. Young's modulus measured with spherical micro-indentation are more representative of the mechanical behavior of porous alumina supports.

4.1.3 Impact of microstructural characteristics on mechanical properties of alumina supports

The three alumina supports have similar total porosity fraction and the measurement of their specific surfaces and their pore size distribution indicates only slight differences (*Table 1*). Results of micro-indentation and three point bending tests show that Young's modulus obtained on the support MD is twice higher than the support THD and slightly higher than the support HD (*Table 5*). The same tendency is observed of the maximum tensile stress at fracture and the experimental pressure corresponding to damage initiation (*Figure 7*). Elastic properties and mechanical strength may be highly influenced by the microstructural morphology. Actually, each of them is composed of grains dispersed randomly in the matrix. It can be noted that the alumina support THD which has the lowest fraction of grains (2.5 %, Table 2, *Figure 5*), exhibits the least mechanical properties. The alumina support THD is characterized by a higher dispersion, that means the majority of boehmite agglomerates were dissociated to form matrix, explaining the low volume fraction of grains. On the contrary, the support MD heterogeneity results from a low dispersibility of boehmite agglomerates. The mechanical properties of alumina supports are thus highly affected by the degree of agglomerates dispersion during the fabrication.

The scatter of results is much more important for the alumina support HD in bending testing as well as in micro-indentation testing (*see Table 4, Table 5*) than the supports MD and THD, which could be explained by the presence of more heterogeneities and large defects. Large defects were noted during SEM observation of longitudinal cross-sections of alumina supports. As it can be seen in *Figure 14.a*, these defects can be surface defects, axial cracks or local density variations in the matrix running along the extrudate length. These kinds of defects were not observed on the microstructure

of support MD. This observation could explain the intermediate mechanical strength of the support HD (*see Table 4*) despite the heterogeneous microstructure.

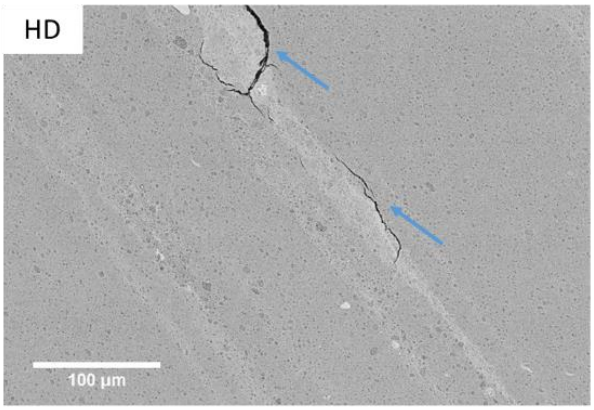

Figure 14: SEM observation of vertical cuts of alumina support "HD". The direction of extrusion corresponds to the direction of white lines (densified zones running along the extrudate length). Arrows indicate defects.

4.2 Local mechanical behavior of grains and matrices

4.2.1 Impact of porosity and microstructure characteristics

Thanks to the estimation of the local porosity of grains and matrices (section 3.1.3) and to the results of nano-indentation (section 3.5), local porosities were drawn against Young's Modulus and hardness of grains and matrices.

The measurement of contact area from SEM images gives hardness values smaller (typically by 20%) as compared to CSM values listed in Table 7 for both matrices and grains. The precise determination of the projected area of contact is delicate from imaging at high magnification. Therefore the parameters extracted from indenters at small penetration of these highly porous materials are considered as mainly for comparison purposes between matrices and grains.

Figure 15 shows that grains are stiffer and harder than matrix. Measurements from tests in grains may be influenced to some degree by the surrounding and underlying materials. The properties of grains for indentation tests could then be underestimated by the presence of the surrounding matrix. The possible influence of the matrix on the determination of grain properties is supposed to be limited by the choice of the maximum indentation depth (i.e., residual imprint depth from 300 to 350 nm for an average grain size ranging from 1 to 3 µm) and by the fact that matrices are at maximum two times softer and three times less hard than the grains, i.e., with values in a similar order of magnitude.

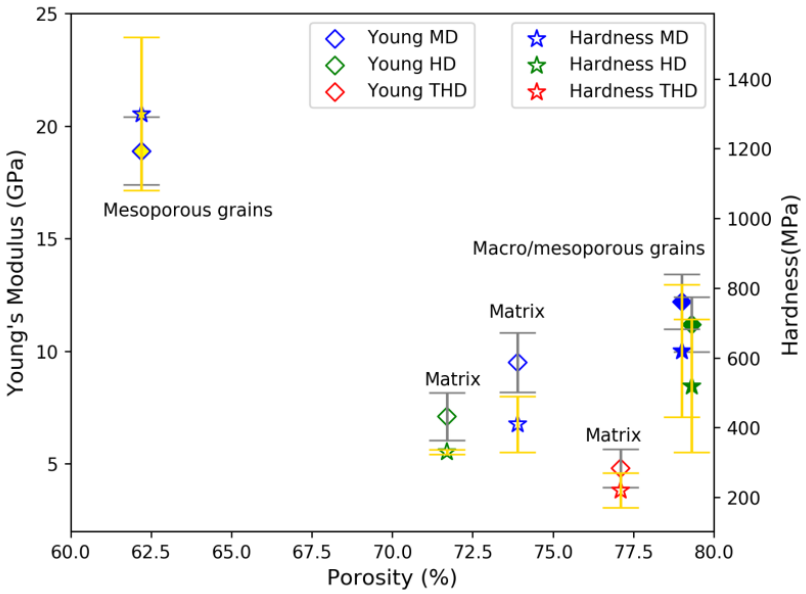

Figure 15: Relationship between Young's modulus and hardness values of grains and matrix of the three alumina supports versus their volume fraction of porosity.

For the alumina support MD, meso-porous grains with the lower porosity fraction (estimated to 62.2%, *see Table 2*), are stiffer than macro-meso-porous grains and matrix. Logically, the increase of the volume fraction porosity leads to the decrease of mechanical properties [40] which could explain the highest mechanical properties of the meso-porous grains. In spite of a larger porosity, macro-and meso-porous grains exhibit a higher mechanical strength than the matrices. A beneficial organization of the porous network and a higher cohesion of alumina nanocrystals may explain this higher strength, as discussed hereafter.

4.2.2 Impact of agglomerates dispersibility on porous network

Macro-and meso-porous grains tested in nano-indentation are agglomerates, presented in *Figure 1*. These grains are resistant to chemical dispersion and so to the physical and mechanical action necessary to break down aggregates. Inside these agglomerates, aggregates are strongly bounded due to electrostatic and physical forces (Van de Waals forces, hydrogen bonding). The strong cohesion between aggregates could explain the high mechanical properties of grains as compared to matrix, as noted for all three materials. Due to their relatively high mechanical properties, the presence of macro and meso-porous grains in the microstructure could enhance the mechanical properties of the alumina support. However, according to the *Table 2*, catalyst supports are composed of a high volume fraction of matrix (higher than 85 %) which indicates that the mechanical properties of catalyst supports are strongly affected by the mechanical properties of matrix. The mechanical effect of the matrix on the strength of alumina support have been identified by comparing normalized hardness $H_{Berko}/H_{Berko}(THD)$ measured by Berkovich micro-indentation to normalized hardness $H_{Berko}/H_{Berko}(THD\ matrix)$ measured by Berkovich nano-indentation of matrices. It has been noted that normalized hardness obtained by micro and nano-indentation are similar which indicates that the mechanical behavior of alumina supports is controlled by the mechanical properties of matrix.

Table 8: Normalized Berkovich hardness measured by micro-indentation and nano-indentation

Alumina support	Micro-indentation Normalized H_{Berko}	Nano-indentation Normalized H_{Berko}(matrix)
MD	1.87	1.86
HD	1.53	1.50
THD	1	1

Furthermore, it has been shown that matrices of the three alumina supports which have almost similar porous volume fraction, exhibit different mechanical properties as presented in *Figure 15*. In fact, matrices of the three materials do not have a similar microstructural morphology (size and shape of nanocrystal for instance) since matrices were synthesized with different conditions (type and quantity of acid for the dispersion step) [19]. SEM observations in Figure 3 indicates that matrices of the three alumina supports tested by nano-indentation have different microstructure. The matrix of the support MD is the most heterogeneous composed of different small grains which could enhance the mechanical behavior of the matrix.

4.2.3 Relationships between global and local mechanical behaviour

The mean values of Young's modulus and hardness obtained by nano-indentation of grains and matrices (

Table 7) were calculated. Compared to elastic properties measured with Berkovich micro-indentation (*Table 6*), the mean values of local elastic properties are slightly higher. In fact, with deep indentation tests, a highly volume of alumina is tested and so the results are more susceptible to macro defects such as cracks, less dense areas, decohesion between grains and matrix which could affect the Young's modulus of the alumina supports.

Moreover, results of shallow indentations could be affected by the phenomena referred as "Indentation Size Effect" (ISE). During the indentation test, the maximum applied load, or the maximal penetration depth, can influence the hardness: hardness decreases while increasing applied indentation load. This phenomena is usually observed in metals [42] but also in ceramics [43]. For alumina catalyst supports, the evolution of Berkovich hardness with maximum penetration depth (for different applied loads) is shown in *Figure 16*. The hardness was found independent on loads at around 3 µm of maximal penetration depth (ISE boundary). Several explanations for the indentation size effect have been proposed. An approach based on the energy balance consideration was proposed firstly by [44] and developed by [45]. In this approach, the work of indentation is converted in energy consumed in local damage and plastic mechanisms, as well as in fracture propagation. ISE originates in the fact that at low loads, local irreversible deformation (plasticity, microcracking) is the controlling process while at higher loads, cracking is favored and can affect the measured hardness. As a consequence, the hardness value varies with indent's depth, as shown in *Figure 16*. Absolute

values of hardness measured in micro and nano- indentation tests are therefore not directly comparable. The relative values for the different materials can however be compared (see here above).

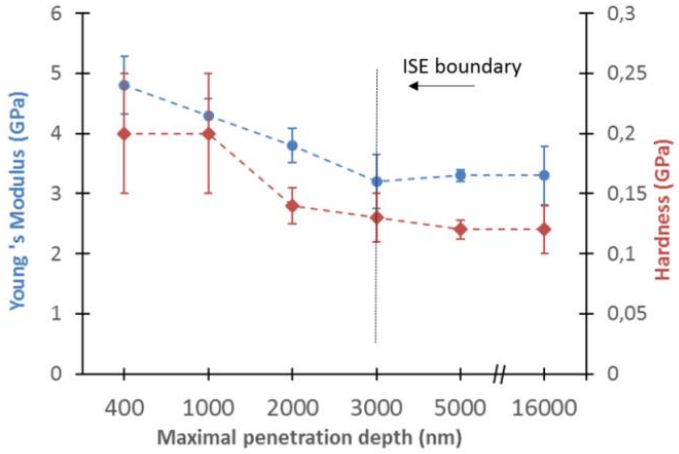

Figure 16: The hardness of the alumina support "THD" as a function of the maximal indentation penetration depth showing ISE boundary where the hardness become independent on loads

5 Conclusion

Three alumina supports of similar porous volume fraction (70%) and mean interconnection pore size (9 nm) are studied. The three materials are composed by grains dispersed in a matrix, each being made of γ-alumina at different porosity fractions. The alumina supports are distinguished by different degrees of agglomerates dispersion, which means different volume fraction of grains. When the dispersion is more important, the volume fraction of grains is lower in the final material. Several conclusions can be drawn from this study:

(1) Alumina supports exhibit quasi-plastic damage under triaxial compression commonly observed in highly porous ceramics using micro-indentation tests. Similar behavior is noted at local scale by nano-indentation tests. The quasi plasticity of porous alumina supports is reflected by the absence of cracks around the residual indent indicating a damage caused by collapse of pores and densification of the material.

(2) Nano-indentation tests as shallow as 400 nm have provided mechanical properties of grains and matrix constituting the microstructure of alumina supports. The mean values of local properties are higher than values measured with Berkovich micro-indentation. It has been shown that the local values could be affected by ISE phenomena.

(3) Local porosities fractions in matrix and grains were estimated via image processing on SEM images of polished surface of alumina supports. Thanks to this, it has been shown that macro-and meso-porous grains, even if more porous than matrix, are stiffer and harder. This discrepancy is explained by the strong physical and chemical cohesion between alumina aggregates inside grains. The mechanical properties of alumina supports are strongly affected by the microstructure, which is influenced by the dispersion of the material during the fabrication. It has been shown that the mechanical behavior of alumina supports is mainly controlled by the mechanical properties of their matrix. In this study, TEM could be

useful to estimate the morphology of aggregates and nanocrystals composing matrices. However, a delicate FIB milling need to be performed on the alumina support in order to obtain an ultrathin specimen of the matrix with a thick less than 100 nm required for TEM observation.

Acknowledgements

The authors would like to acknowledge the CLYM (Centre Lyonnais de Microscopie) for the access to SEM supra 40 and to the microscope FIB ZEISS. The authors are grateful to Thierry Douillard (CLYM) for his contribution to realize the FIB cross-section of nano-indentation imprint. Thanks to Vincent Lecocq in the department “GMD” at IFP Energies nouvelles (Solaize, France) for the preparation of the alumina supports and Loïc Sorbier in the department “Caractérisation matériaux” at IFP Energies nouvelles (Solaize, France) for his help to analyze porosity via SEM images.

6 References

[1] K. Wefers, "Alumina Chemicals Science and Technology Handbook”.
[2] M.S. Rana, J. Ancheyta, S.K. Maity, P. Rayo, Hydrotreating of Maya Crude Oil, Petroleum Science and Technology 25 (2011) 187–199.
[3] D. Wu, J. Zhou, Y. Li, Mechanical strength of solid catalysts, AIChE J. 53 (2007) 2618–2629.
[4] S.P.S. Andrew, Theory and practice of the formulation of heterogeneous catalysts, Chemical Engineering Science 36 (1981) 1431–1445.
[5] A.A. Griffith, The Phenomena of Rupture and Flow in Solids, Philosophical Transactions of the Royal Society A: Mathematical, Physical and Engineering Sciences 221 (1921) 163–198.
[6] D. Staub, S. Meille, V. Le Corre, J. Chevalier, L. Rouleau, Revisiting the Side Crushing Test Using the Three-Point Bending Test for the Strength Measurement of Catalyst Supports, Oil Gas Sci. Technol. – Rev. IFP Energies nouvelles 70 (2015) 475–486.
[7] D. Staub, S. Meille, V. Le Corre, L. Rouleau, J. Chevalier, Identification of a damage criterion of a highly porous alumina ceramic, Acta Materialia 107 (2016) 261–272.
[8] S. Meille, M. Lombardi, J. Chevalier, L. Montanaro, Mechanical properties of porous ceramics in compression: On the transition between elastic, brittle, and cellular behavior, Journal of the European Ceramic Society 32 (2012) 3959–3967.
[9] M.F. Ashby, C.G. Sammis, The damage mechanics of brittle solids in compression, PAGEOPH 133 (1990) 489–521.
[10] F.-J. Ulm, M. Vandamme, C. Bobko, J. Alberto Ortega, K. Tai, C. Ortiz, Statistical Indentation Techniques for Hydrated Nanocomposites, J American Ceramic Society 90 (2007) 2677–2692.
[11] K.C. Bennett, L.A. Berla, W.D. Nix, R.I. Borja, Instrumented nanoindentation and 3D mechanistic modeling of a shale at multiple scales, Acta Geotech. 10 (2015) 1–14.
[12] P. Clément, S. Meille, J. Chevalier, C. Olagnon, Mechanical characterization of highly porous inorganic solids materials by instrumented micro-indentation, Acta Materialia 61 (2013) 6649–6660.
[13] Brian R. Lawn, Indentation of Ceramics with Spheres: A Century after Hertz (1998).
[14] G. Constantinides, On the use of nanoindentation for cementitious materials, Mater. Struct. 36 (2003) 191–196.

[15] G. Constantinides, K.S. Ravi Chandran, F.-J. Ulm, K.J. van Vliet, Grid indentation analysis of composite microstructure and mechanics, Materials Science and Engineering: A 430 (2006) 189–202.
[16] H. Buckle, L'essai de microdureté et applications, 1960.
[17] M. Miller, C. Bobko, M. Vandamme, F.-J. Ulm, Surface roughness criteria for cement paste nanoindentation, Cement and Concrete Research 38 (2008) 467–476.
[18] A.R. Sakulich, V.C. Li, Nanoscale characterization of engineered cementitious composites (ECC), Cement and Concrete Research 41 (2011) 169–175.
[19] D. Chiche, M. Digne, R. Revel, C. Chanéac, J.-P. Jolivet, Accurate Determination of Oxide Nanoparticle Size and Shape Based on X-Ray Powder Pattern Simulation, J. Phys. Chem. C 112 (2008) 8524–8533.
[20] L. Roiban, L. Sorbier, C. Pichon, C. Pham-Huu, M. Drillon, O. Ersen, 3D-TEM investigation of the nanostructure of a δ-Al2O3 catalyst support decorated with Pd nanoparticles, Nanoscale 4 (2012) 946–954.
[21] S. Brunauer, P.H. Emmett, E. Teller, Adsorption of Gases in Multimolecular Layers (1938).
[22] E.P. Barrett, L.G. Joyner, P.P. Halenda, The Determination of Pore Volume and Area Distributions in Porous Substances. I. Computations from Nitrogen Isotherms (1951).
[23] J. Schindelin, I. Arganda-Carreras, E. Frise, V. Kaynig, M. Longair, T. Pietzsch, S. Preibisch, C. Rueden, S. Saalfeld, B. Schmid, J.-Y. Tinevez, D.J. White, V. Hartenstein, K. Eliceiri, P. Tomancak, A. Cardona, Fiji: an open-source platform for biological-image analysis, Nature methods 9 (2012) 676–682.
[24] L. Reimer, H. Kohl, Transmission electron microscopy: Physics of image formation, 5th ed., Springer, New York NY, 2008.
[25] L.R. R. Herrmann, Backscattering coefficient of multicomponent specimens.
[26] D. BERGER AND H. NIEDRIG, Complete angular distribution of electrons backscattered from tilted multicomponent specimens.
[27] C.J.L. Lemaitre J., Mécanique des milieux continus, Dunod, 2nd ed., Paris, (2004).
[28] W.C. Oliver, G.M. Pharr, An improved technique for determining hardness and elastic modulus using load and displacement sensing indentation experiments, J. Mater. Res. 7 (1992) 1564–1583.
[29] M.F. Doerner, W.D. Nix, A method for interpreting the data from depth-sensing indentation instruments, J. Mater. Res. 1 (1986) 601–609.
[30] J.S. Field, M.V. Swain, A simple predictive model for spherical indentation, J. Mater. Res. 8 (1993) 297–306.
[31] I.N. Sneddon, The relation between load and penetration in the axisymmetric boussinesq problem for a punch of arbitrary profile, International Journal of Engineering Science 3 (1965) 47–57.
[32] W.C. Oliver, G.M. Pharr, Measurement of hardness and elastic modulus by instrumented indentation, J. Mater. Res. 19 (2004) 3–20.
[33] S.I. Bulychev, V.P. Alekhin, M.K. Shorshorov, A.P. Ternovskii, G.D., Mechanical properties of materials studied from kinetic diagrams of load versus depth of impression during microimpression (1975).
[34] L.-H. He, O.C. Standard, T.T.Y. Huang, B.A. Latella, M.V. Swain, Mechanical behaviour of porous hydroxyapatite, Acta biomaterialia 4 (2008) 577–586.

[35] A. Bouterf, S. Roux, F. Hild, J. Adrien, E. Maire, S. Meille, Digital Volume Correlation Applied to X-ray Tomography Images from Spherical Indentation Tests on Lightweight Gypsum, Strain 50 (2014) 444–453.
[36] Z. Chen, X. Wang, A. Atkinson, N. Brandon, Spherical indentation of porous ceramics, Journal of the European Ceramic Society 36 (2016) 1435–1445.
[37] J.J. Schwiedrzik, P.K. Zysset, The influence of yield surface shape and damage in the depth-dependent response of bone tissue to nanoindentation using spherical and Berkovich indenters, Computer methods in biomechanics and biomedical engineering 18 (2015) 492–505.
[38] S. Pathak, S.R. Kalidindi, Spherical nanoindentation stress–strain curves, Materials Science and Engineering: R: Reports 91 (2015) 1–36.
[39] B. Benane, S. Meille, G. Foray, B. Yrieix, C. Olagnon, Instrumented Indentation of Super-Insulating Silica Compacts, Materials (Basel, Switzerland) 12 (2019).
[40] R.L. Coble, W.D. Kingery, Effect of Porosity on Physical Properties of Sintered Alumina (1956).
[41] Haisheng Wang, Morphological Modelling and Transport Properties of Mesoporous Alumina, 2016.
[42] Q. Ma, D.R. Clarke, Size dependent hardness of silver single crystals, J. Mater. Res. 10 (1995) 853–863.
[43] S.J. Bull, T.F. Page, E.H. Yoffe, An explanation of the indentation size effect in ceramics, Philosophical Magazine Letters 59 (1989) 281–288.
[44] Fröhlich, F., P. Grau, and W. Grellmann, Performance and analysis of recording microhardness tests (1977).
[45] G.Q. J.B. Quinn, Indentation brittleness of ceramics: a fresh approach Journal of materials science 4331-4346 (1997).